Supplemental Material:

Molecular tail chemistry controls thermal transport in fullerene films

Ashutosh Giri,[1,*] Stanley S. Chou,[2] Daniel E. Drury,[2] Kathleen Q. Tomko,[3]
David Olson,[1] John T. Gaskins,[1] Bryan Kaehr,[2] and Patrick E. Hopkins[1,3,4,†]

[1]*Department of Mechanical and Aerospace Engineering,*
University of Virginia, Charlottesville, Virginia 22904, USA

[2]*Advanced Materials Laboratory, Sandia National Laboratories,*
Albuquerque, New Mexico 87185, USA

[3]*Department of Materials Science and Engineering,*
University of Virginia, Charlottesville, Virginia 22904, USA

[4]*Department of Physics, University of Virginia, Charlottesville, Virginia 22904, USA*

I. ANALYSIS OF TIME DOMAIN THERMOREFLECTANCE

Cahill derived an expression for the temperature change on a metal surface due to laser heating, $\theta(r)$, where r is the radial coordinate, assuming radial spreading of heat in a half-sphere due to the pump pulse from the axially symmetric heat equation in cylindrical coordinates given by,

$$C\frac{\partial\theta(r,z,t)}{\partial t} = \lambda_z\frac{\theta(r,z,t)}{\partial z^2} + \frac{\lambda_r}{r}\frac{\partial}{\partial r}\left(r\frac{\partial\theta(r,z,t)}{\partial r}\right) \tag{1}$$

where λ is the thermal conductivity, the subscripts r and z denote radial and cross-plane conductivities, and C is the heat capacity. For a multilayered stack, the boundary conditions (for example at the film/substrate interface) are given by,

$$-\lambda_{1,2}\frac{\partial\theta_{1,2}(r,z,t)}{\partial z} = G_{12}(\theta_1(r,z,t) - \theta_2(r,z,t)) \tag{2}$$

where subscripts 1 is for the film and 2 is for the substrate and G is the thermal boundary conductance.

Due to the cylindrical symmetry, we apply the Hankel transform for Eq. 1 in the r and z dimensions, then we apply a Fourier transform, which leads to

$$\frac{\partial^2\theta(r,z,\omega)}{\partial z^2} = q^2\theta(r,z,\omega) \tag{3}$$

where ω is the angular frequency and

$$q^2 = \frac{\lambda_r k^2 + iC\omega}{\lambda_z} \tag{4}$$

where k is the transform variable. For this work, as we are considering isotropic materials, we are only interested in the cross-plane properties, so $q = \sqrt{k^2 + (iC\omega)/\lambda_z}$.

The temperature change in the surface due to heat flow through the underlying materials for steady periodic temperature in the composite slabs is given for the change in surface temperature of material 1,[1]

$$F(k) = \frac{1}{\gamma_1}\left(\frac{F_{T1}^{+} + F_{T1}^{-}}{F_{T1}^{-} - F_{T1}^{+}}\right) \tag{5}$$

where $\gamma = \lambda_z q$, and F_{T1}^{+} and F_{T1}^{-} are temperature change coefficients related to the forward and backward propagating waves on the surface of material 1. The propagating waves in the top layer are related to the waves in the bottom layer through,

$$\begin{pmatrix} F_{T1}^{+} \\ F_{T1}^{-} \end{pmatrix} = \begin{pmatrix} \exp[-q_1 d_1] & 0 \\ 0 & \exp[q_1 d_1] \end{pmatrix}\begin{pmatrix} F_{B1}^{+} \\ F_{B1}^{-} \end{pmatrix} \tag{6}$$

where d is the materials thickness. Given a thermal boundary conductance, the temperature at the top of material 2 is related to the temperature at the bottom of material 1 by

$$\begin{pmatrix} F_{B1}^{+} \\ F_{B1}^{-} \end{pmatrix} = \frac{1}{2} \begin{pmatrix} 1+\frac{\gamma_2}{\gamma_1}-\frac{\gamma_2}{G_{12}} & 1-\frac{\gamma_2}{\gamma_1}+\frac{\gamma_2}{G_{12}} \\ 1-\frac{\gamma_2}{\gamma_1}-\frac{\gamma_2}{G_{12}} & 1+\frac{\gamma_2}{\gamma_1}+\frac{\gamma_2}{G_{12}} \end{pmatrix} \begin{pmatrix} F_{T2}^{+} \\ F_{T2}^{-} \end{pmatrix} \tag{7}$$

As we consider a bulk substrate, heat can not reach the bottom side of the substrate at the rates comparable to the modulation frequency and therefore there is no thermal build up of waves, so

$$\begin{pmatrix} F_{T2}^{+} \\ F_{T2}^{-} \end{pmatrix} = \begin{pmatrix} 0 \\ \exp[-q_2 d_2] \end{pmatrix} \tag{8}$$

Next, to determine the temperature oscillations on the surface of material 1 due to cooling from the underlying layers, we convolute Eq. 5 with the guassian pump beam distribution, which gives

$$\theta(k) = F(k)\frac{A}{2\pi}\exp\left[\frac{-k^2 w_0^2}{8}\right]. \tag{9}$$

where w_0 is the $1/e^2$ pump beam radius. Then, taking the weighted average of the surface temperature oscillations by the probe beam with radius w_1, we get

$$\theta(r,0,\omega) = \frac{A}{2\pi}\int_0^\infty F(k)\exp\left[\frac{-k^2(w_0^2+w_1^2)}{8}\right]kdk \tag{10}$$

This gives the change in temperature as a function of heating event modulation frequency at the surface of the film and is called the axially symmetric frequency-domain model.[2]

We measure the probe thermoreflectance response through a lock-in amplifier, which can detect small changes in the voltage; the change in the thermoreflectance due to the pump heating is $\sim 10^{-4}$ K^{-1}. The output of the lock-in amplifier relates the frequency-domain to the time-domain through the magnitude R and phase ϕ at the heating even modulation frequency given by

$$R\exp[i(\omega_0 t+\phi)] = Z(\omega_0)\exp[i\omega_0 t], \tag{11}$$

where ω_0 is the modulation frequency of the pump pulses and $Z(\omega_0)$ is the transfer function of the lock-in represented as,[3]

$$Z(\omega_0) = \frac{(2\pi)^2\chi}{\omega_s^2}\sum_{M=-\infty}^{\infty}\theta(\omega_0+M\omega_s)\exp[iM\omega_s\tau], \tag{12}$$

where we get θ from the frequency-domain model, ω_s is the modulation frequency of the Ti:Al_2O_3 oscillator ($\omega_s = 2\pi \times 80$ MHz), τ is the delay time between pump and probe pulses, and χ is a constant that is related to the gain of the electronics, the power of the pump and probe pulses, and the thermoreflectance coefficient of the material.[2] The thermoreflectance of a material is related to its electronic band structure, transitions and its dielectric function.

II. STEADY-STATE THERMOREFLECTANCE MEASUREMENTS

We use a fiber-optic integrated steady-state thermoreflectance (SSTR) system to measure the thermal conductivity of the 3 μm PCBM sample, independent of its volumetric heat capacity. Specific details regarding SSTR can be found in Braun *et al.*'s work.[4] Briefly, we use a continuous wave (cw) fiber-coupled 637 nm diode laser as the pump, digitally modulated using the output of our lock-in amplifier at 100 Hz to create heating event at the sample surface. A cw fiber-coupled 785 nm diode laser is used to probe this heating event by monitoring changes in thermoreflectance of the aluminum transducer layer at the sample surface. A linear dependence of the probe response as a function of increasing pump power can be compared to the heat diffusion equation to determine the thermal conductivity of PCBM. The fiber optic components used in our implementation parallel those of their free space counterparts, allowing us to entirely encompass the system in fiber optics, except for when collinearly collimating the pump and probe for focusing on the sample surface using a 20× objective. We use an automated focusing routine, ensuring a consistent effective 1/e^2 pump/probe radii ($3\pm0.15\mu$m), over a 1×1 mm region in which a random coordinate pair in each of the 500×500 μm subregions is chosen as the sampling point, resulting in a total of four samples. The total time for these four samples was <5 min.

Prior to these SSTR measurements, we perform a frequency domain thermoreflectance (FDTR) scan to examine the frequency-dependency of the pump heating even to determine whether or not our steady-state analysis is justified at 100 Hz. The magnitude of this FDTR scan is shown in Fig. S1(a), where the data are normalized to our lowest frequency, 100 Hz. The leveling out of the signal below $\sim$1e3 Hz is indicative of the fact that the sample is effectively in a steady-state regime, allowing us to perform measurements at 100 Hz to determine the thermal conductivity of PCBM independent of its volumetric heat capacity. The fact that the system reaches steady state at these frequencies is due to the high thermal conductivity of the Si substrate.

SSTR measurements are shown in Fig. S1(b) for the Al/PCBM/Si specimen, as well as an

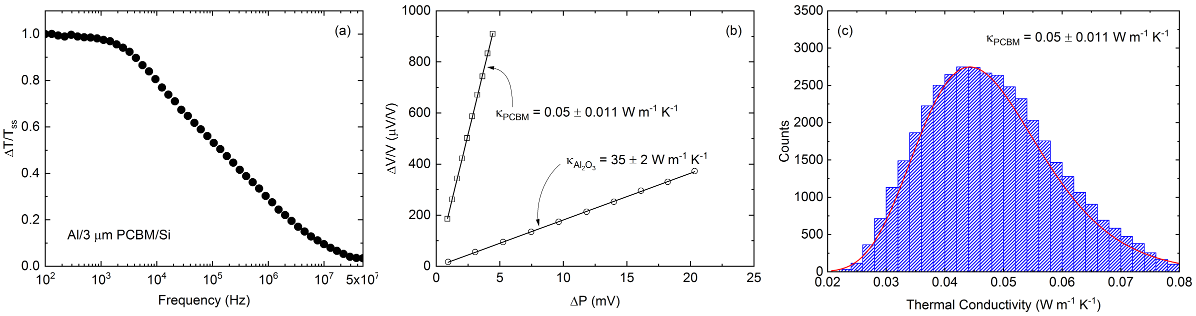

Figure S1. (a) Magnitude of frequency domain thermoreflectance data for our Al/3 μm PCBM/Si sample, normalized at 100 Hz. (b) Representative SSTR data for the Al/Al$_2$O$_3$ reference specimen and Al/3 μm PCBM/Si sample. The increased probe magnitude ($\Delta V/V$) for smaller pump magnitude (ΔP) of the Al/3 μm PCBM/Si sample is indicative of a greater amount of heating due to the insulating nature of PCBM. (c) Monte Carlo uncertainty analysis for the Al/3 μm PCBM/Si specimen over four sampling points. The routine is performed for 10^4 iterations for each sampling point, yielding a total of 4×10^4 points in the distribution used to acquire both the mean value and uncertainty of the thermal conductivity of PCBM.

Table S1. Parameters used in SSTR analyses for determination of γ using the Al$_2$O$_3$ reference as well as the thermal conductivity of PCBM. Uncertainties of known parameters are inputted into a Monte Carlo approach for the extraction of the desired parameters and their uncertainties.

Layer	Thickness (nm)	Thermal conductivity (W m^{-1} K^{-1})	Volumetric Heat capacity (J cm^{-3} K^{-1})	G (MW m^{-2} K^{-1})
Al	79±2	95±5	2.42±0.06	200±20
Al$_2$O$_3$	-	35±5	3.06±0.08	
Al	82±2	126±4	2.42±0.06	50±13
PCBM	3000±100	-	1.34±1.00	50±13
Si	-	140±35	1.60±0.04	

Al/Al$_2$O$_3$ reference specimen with which we use to determine γ, the proportionality constant by which we relate our SSTR magnitude to our thermal model.[4] We use a Monte Carlo routine using 10^5 iterations to determine the uncertainty associated with γ, based on uncertainties in the known parameters of our Al/Al$_2$O$_3$ reference specimen. These known parameters and their uncertainties are tabulated in Table S1. Ultimately, this results in a standard deviation of 5% of the mean for γ.

Using our SSTR fiber optic system, we determine the thermal conductivity of PCBM to be 0.05±0.011 W m^{-1} K^{-1}, in good agreement with the value derived from TDTR. We note that we are entirely insensitive to the volumetric heat capacity of the fullerene derivative—we can adjust the volumetric heat capacity from 0.05 to 5 MJ m^{-3} K^{-1} and achieve the same result. The uncertainty is representative of one standard deviation from the acquired distribution using a Monte Carlo routine with 10^4 iterations per sampling point, where the parameters used are presented in Table S1 and the distribution is shown in Fig. S1(c). This routine is similar to that employed to extract γ. We note that the thermal conductivity and thickness of the Al transducer, as well as the $1/e^2$ pump/probe radii will have the most prominent effect on our thermal model for this specimen configuration, and it is the uncertainty of these parameters that primarily contributes to that of the extracted thermal conductivity of PCBM. Spot to spot variations account for a contribution of just 4% to the overall uncertainty.

III. SAMPLE CHARACTERIZATION

We measure heat capacity of our PCBM directly using Differential Scanning Calorimetry (DSC). A Netzsch Polyma DSC was calibrated with sapphire and PCBM was characterized in an argon environment. As shown in Fig. S4, the first run from 0-500 °C resulted in a endothermic peak at 275 °C followed by an exothermic dip starting at 350 °C. This could be a result of volatilization of the side change (TGA measurements are in progress) or, more likely, a melting followed by crystallization phase change. In any case, the room temperature heat capacity falls within the range of reported values for PCBM.

IV. ATOMISTIC SIMULATIONS

A. Polymer consistent force field

The polymer consistent force field potential is a general all-atom force field that includes the van der Waals force, bond angles, dihedrals, and improper interactions, which has been extensively used to model organic and inorganic small molecules.[5,6] The form of the potential is given as,

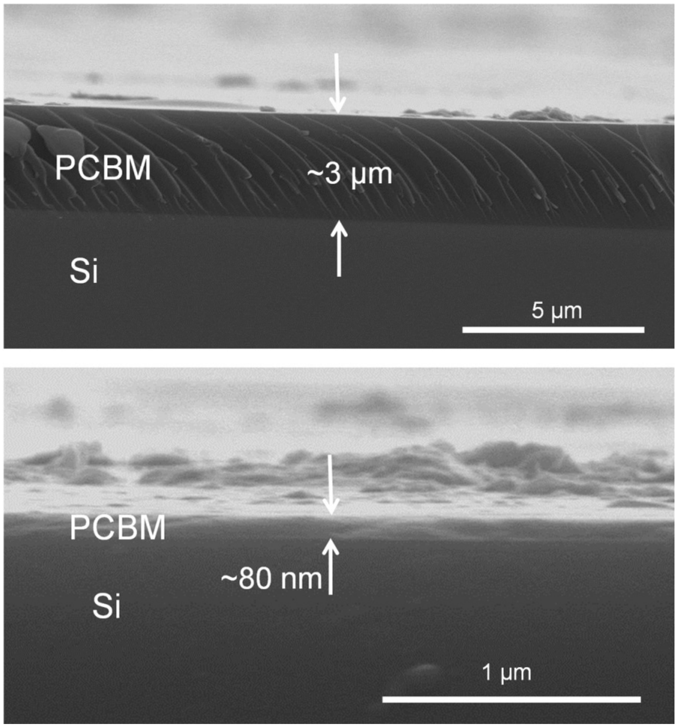

Figure S2. Scanning electron micrograph (SEM) cross-section of a cast (top panel) and spin-coated (bottom panel) PCBM material on silicon substrate.

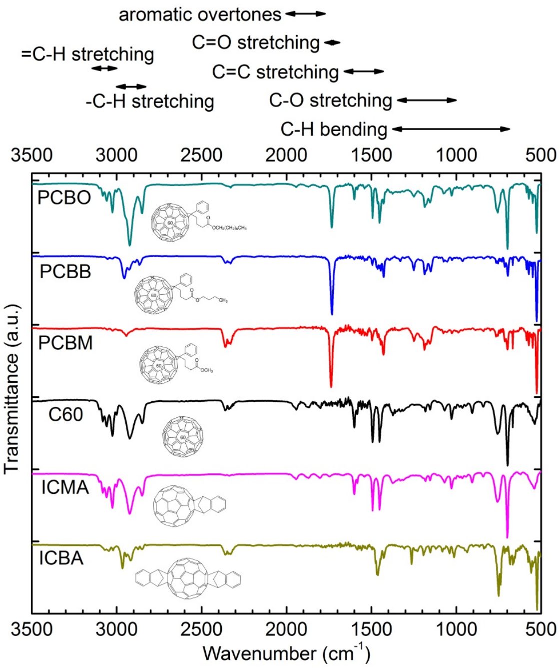

Figure S3. Annotated FTIR spectra of the fullerene materials used in this work.

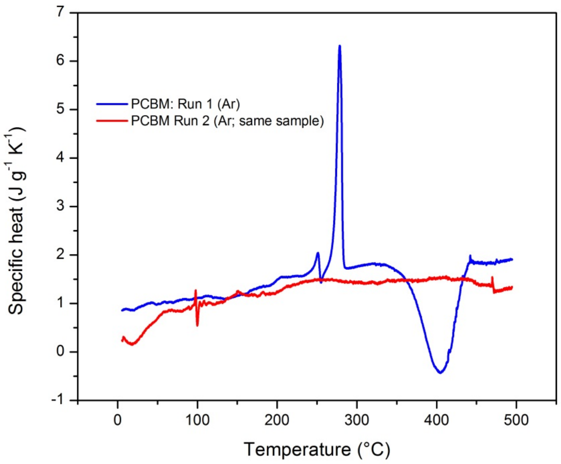

Figure S4. Specific heat of PCBM from 0-500 °C measured with DSC.

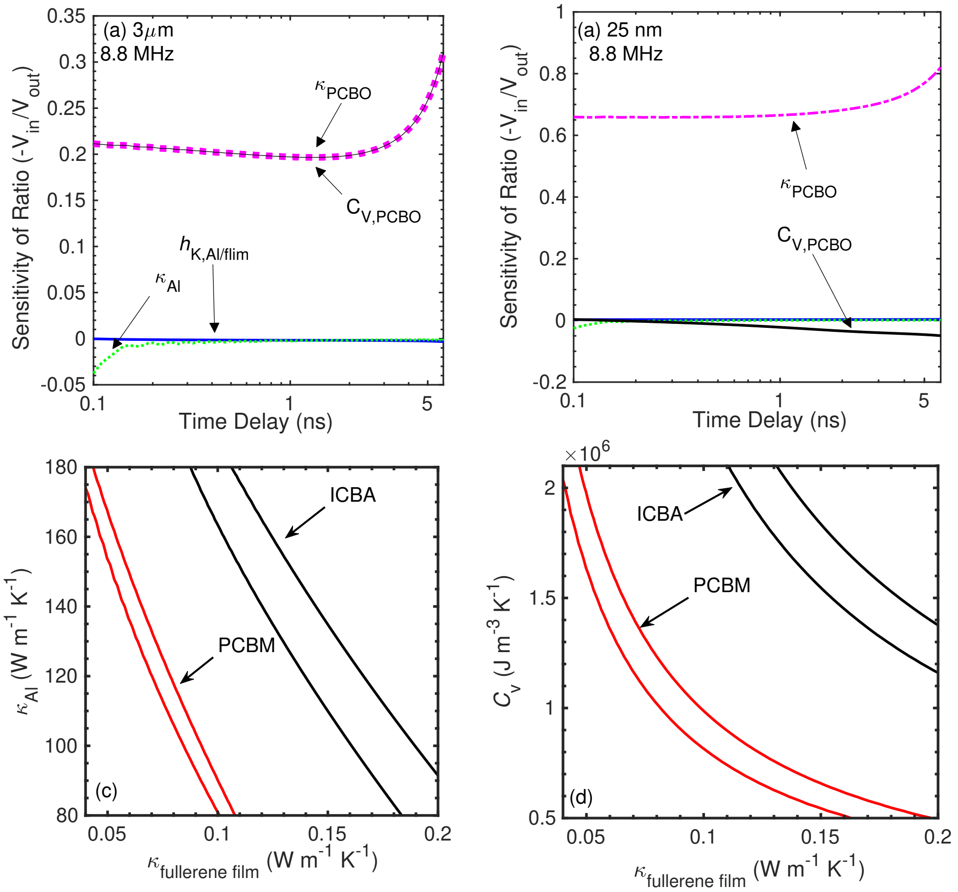

Figure S5. Sensitivities of the ratio of the in-phase and out-of-phase signals to the parameters used in the thermal model for a (a) 3 μm and (b) 25 nm thick PCBO sample. (a) Sensitivity contour plots showing the interrelationship between the thermal conductivity of aluminum and the thermal conductivity thick fullerene films. The thermal conductivity of aluminum is 126±6 W m^{-1} K^{-1}, which is measured using the four-point probe method. (b) Sensitivity contour plots showing the interrelationship between heat capacity and thermal conductivity of thick fullerene films. The lines represent twice the sum of the standard deviation between the thermal model prediction and the experimentally measured data that represents the 95 % confidence level.

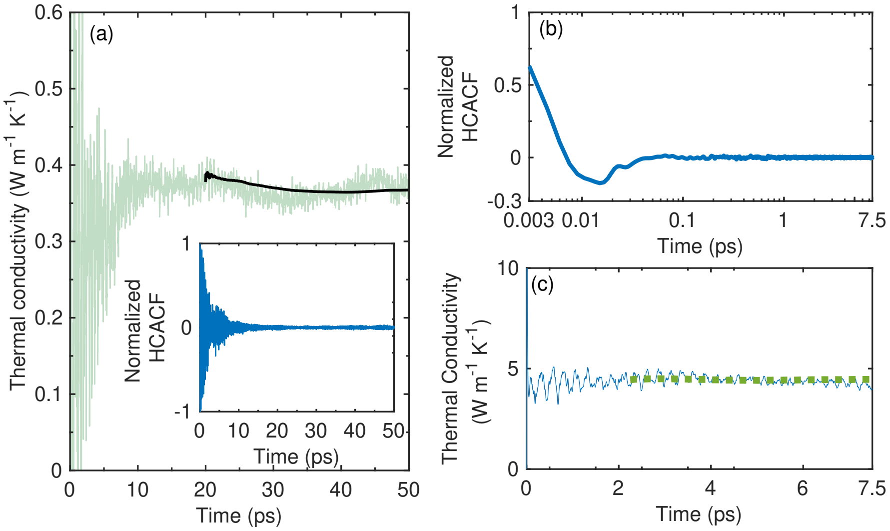

Figure S6. Green-Kubo predicted thermal conductivity of an fcc fullerene crystal. (inset) HCACF vs. time for the fullerene crystal showing that the integration time of 50 ps is enough to provide a converged thermal conductivity. (b) HCACF vs. time and (c) the converged thermal conductivity for amorphous carbon predicted via the Green-Kubo method.

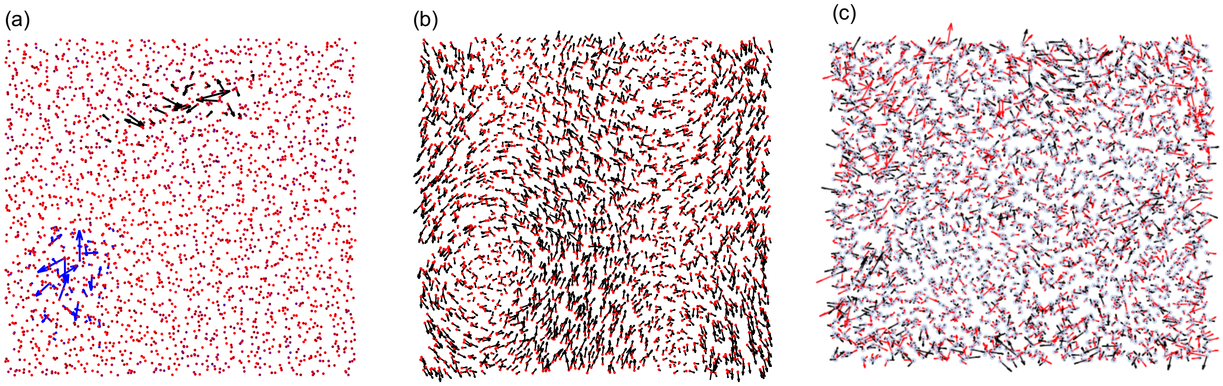

Figure S7. Spatial components of the two-dimensional eigenvectors for our amorphous carbon structure showing (a) locons at 59.99 and 60.02 THz frequencies calculated via lattice dynamics calculations. The localized nature of the modes are evident from the lack of spatial overlap between the eigenvectors. (b) Eigenvectors at 3.97 THz showing the propagating nature of the modes at this frequency. (c) Spatial components of the two-dimensional eigenvectors for our amorphous carbon structure showing spatial overlap between the eigenvectors at 10.64 (black arrows) and 10.65 THz (red arrows).

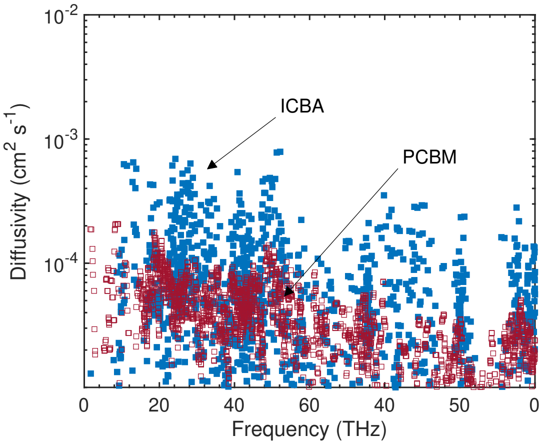

Figure S8. Modal diffusivities calculations from the Allen and Feldman model for our crystalline PCBM and ICBA structures.

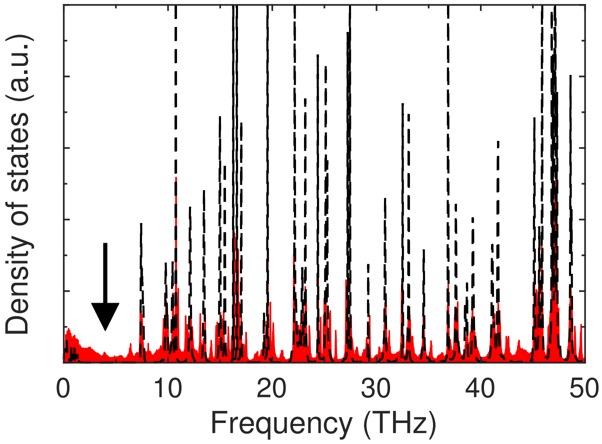

Figure S9. MD-predicted vibrational density of states for the C_{60} (dotted black line) and PCBM (shaded region) structures. The addition of the chain in the PCBM leads to an increase in the density of states of the low frequency modes in the 3-10 THz range that are otherwise absent in the C_{60} crystals as highlighted by the arrow.

$$
\begin{aligned}
E_{\mathrm{tot}} = \sum_{b} \Big[k_2(b-b_0)^2 + k_3(b-b_0)^3 + k_4(b-b_0)^4\Big] \\
(a) \\
+ \sum_{\theta} \Big[D_2(\theta-\theta_0)^2 + D_3(\theta-\theta_0)^3 + D_4(\theta-\theta_0)^4\Big] \\
(b) \\
+ \sum_{\phi} \{V_1 \Big[1 - \cos(\phi-\phi_1) + V_2 \Big[1 - \cos(2\phi - \phi_2)\Big]) + V_3 \Big[1 - \cos(3\phi - \phi_3)\Big] \\
(c) \\
+ \sum_{x} K_x x^2 + \sum_{b,b'} F_{bb'}(b-b_0)(b'-b'_0) + \sum_{b,\theta} F_{b\theta}(b-b_0)(\theta-\theta_0) \\
+ F_{b\phi}(b-b_0)\big[H_1 \mathrm{cos}\phi + H_2 \mathrm{cos}2\phi + H_3 \mathrm{cos}3\phi\Big] \\
+ \sum_{\theta,\phi}(\theta-\theta_0)\big[H_1 \mathrm{cos}\phi + H_2 \mathrm{cos}2\phi + H_3 \mathrm{cos}3\phi\Big] \\
+ \sum_{\theta,\theta'} F_{\theta,\theta'}(\theta'-\theta'_0)(\theta-\theta_0) + \sum_{phi,\theta,\theta'} F_{\phi,\theta,\theta'} \mathrm{cos}\phi(\theta-\theta_0)(\theta'-\theta'_0) \\
(d) \\
+ \sum_{i>,j} \frac{q_i q_j}{r_{ij}} + \sum_{ij} \epsilon_{ij} \left[2\left(\frac{\sigma_{ij}}{r_i j}\right)^9 - 3\left(\frac{\sigma_{ij}}{r_i j}\right)^6\right]\} \\
(e)
\end{aligned}
\tag{13}
$$

B. Computational domain setup, Green-Kubo formalism, and lattice dynamics calculations

Figure. S7a shows the converged value of thermal conductivity of 0.39 W m^{-1} K^{-1} for our C_{60} crystal at 300 K, which is calculated from the integrals of the heat current autocorrelation function shown in the inset of Fig. S7a. Our result is consistent with prior results from GK simulations and also agrees very well with the experimentally measured thermal conductivity of ∼0.4 W m^{-1} K^{-1} at temperatures above 260 K for bulk C_{60} crystals.[7] We note that our previous GK results of ∼0.27 W m^{-1} K^{-1} for C_{60} crystals was obtained with slight variations in the parameterizations of the COMPASS-based interatomic potential utilized in our previous work as compared to

The first term is the covalent bond stretching term (a), the second term is the bond angle term (b), the third term is the dihedral term (c), the fourth term is the harmonic improper term; the terms labeled (d) are the cross-terms that include variations in bond stretching, bending and torsional angle rotation; the last two terms are the Coulumbic electrostatic force and the van der Waals interaction, respectively (e). Table S2 lists the parameters used for our C_{60} structures; all the potential and data file can be provided upon request.

Table S2. Parameters used in Eq. 1 to model the inter- and intra-molecular interactions for C_{60} under the PCFF potential.

b_0 (Å)	k_2 (Kcal/mole/Å^2)	k_3 (Kcal/mole/Å^2)	k_4 (Kcal/mole/Å^2)		
1.4170	470.8361	-627.6179	1327.6345		
θ_0	D_2 (Kcal/mole/rad^2)	D_3 (Kcal/mole/rad^2)	D_4 (Kcal/mole/rad^2)		
118.9000°	61.0226	-34.9931	0.0000		
V_1 (Kcal/mole)	ϕ_1	V_2 (Kcal/mole)	ϕ_2	V_3 (Kcal/mole)	ϕ_3
8.3667	0.0000°	1.1932	0.0000°	0.0000	0.0000°
$F_{bb'}$ (Kcal/mole/Å^2)	$F_{b\theta}$ (Kcal/mole/Å^2)	b_0 (Å)	b'_0 (Å)		
68.2856	28.8708	1.4170	1.4170		
H_1 (Kcal/mol/Å)	H_1 (Kcal/mol/Å)	H_3 (Kcal/mol/Å)			
-0.1185	6.3204	0.0000			
ϵ (Kcal/mole)	σ (Å)				
0.0640	4.0100				

this work. Similarly, Chen *et al.*[8] predicted a thermal conductivity of $\sim$0.2 W m^{-1} K^{-1} with an NEMD approach, which utilized a similar interatomic potential albeit with different parameters for the potential. This suggests that even though similar potentials are used to calculate the thermal conductivities of these systems, differences in the parameterization of the interatomic potential can lead to drastically different results. Therefore, the full parameterization of the PCFF potential used in this work has been tabulated in the supporting information. We note that our MD calculations are classical in nature and do not effectively capture the quantum effects at low temperatures; the contributions of all the phonon modes in the density of states (DOS) of C_{60} are present in our calculations, whereas in the experiments conducted at room temperature, only the modes that are quantum mechanically allowed at that temperature are involved with the heat transfer in C_{60} crys-

Table S3. Molecular dynamics simulations-predicted density, thermal conductivity and heat capacity of the different computational domains studied in this work.

Sample	Density ($\mathrm{g\ cm^{-3}}$)	Thermal conductivity ($\mathrm{W\ m^{-1}\ K^{-1}}$)	Heat capacity ($\mathrm{J\ cm^{-3}\ K^{-1}}$)
a-C	3.19	8.43±0.92	
C_{60}	1.78	0.390±0.04	1.22
PCBM	1.53	0.157±0.013	1.34
bis-adduct PCBM	1.45	0.240±0.020	1.54
PCBB	1.52	0.190±0.016	1.50
PCBO	1.46	0.210±0.015	1.58
bis-adduct PCBO	1.30	0.271±0.025	1.57
ICMA	1.65	0.224±0.018	1.33
ICBA	1.61	0.330±0.036	1.57

tals. Therefore, the thermal conductivity agreement between the experimental results and the MD predictions is likely coincidental.[9] As such, we present the normalized thermal conductivity with respect to the thermal conductivity of PCBM at 300 K in Fig. 3b of the manuscript.

To get an estimate for the heat capacity of the different fullerene derivative films, we calculate the vibrational density of states (DOS) from our MD simulations. The velocities of the atoms in the structures are output every 10 time steps for a total of 1 ns. A velocity autocorrelation function algorithm is used to obtain the local phonon DOS in the various fullerene derivative structures. The density of states, $D(\omega)$, is obtained from the fourier transform ($\mathcal{F}$) of the velocity correlation function (VACF).[10] The Welch method of power spectral density estimation is applied to obtain the $D(\omega)$ and is normalized as follows,

$$D(\omega) = \frac{1}{2} m \mathcal{F}(VACF) \frac{1}{k_{\mathrm{B}} T} \rho \tag{14}$$

where m is the atomic mass, k_{B} is the Boltzmann constant, T is the local temperature, and ρ is the atomic density. Example calculations of DOS for C_{60} and PCBM structures are shown in Fig S9. We use the DOS to calculate the room temperature heat capacity as,

$$C_{\mathrm{V}} = \int_{0}^{\omega_c} \hbar \omega D(\omega) \frac{\partial f}{\partial T} \mathrm{d}\omega, \tag{15}$$

where ω_c is the cutoff frequency, and f is the Bose-Einstein distribution. The estimated values of the different structures at room temperature are given in Table S3.

It should be noted that a direct interpretation of the MD-predicted thermal conductivity based on the Allen-Feldman model should only be carried out if the values of the predicted thermal conductivities agree between the two methods. However, our AF model predictions do not match with those obtained from MD simulations (for example, the MD-predicted thermal conductivity for a-C is 4.7 W m^{-1} K^{-1}, whereas, the AF model predicted thermal conductivity is 2.7 W m^{-1} K^{-1}). The discrepancy may arise from the fact that the MD-predicted thermal conductivity include propagon contributions, whereas the AF-predicted thermal conductivity includes contributions from the diffusons (under the harmonic approximation). Therefore, we note that the main purpose for our AF model calculations is to compare the diffusivities of the modes between a-C, C_{60} and PCBM as shown in Fig. 3f and not to provide a comparative analysis between the thermal conductivity results based on the two methods.

For our Allen-Feldman model, the Lorentzian broadening of the delta function must be several times greater than the average mode spacing, δ_{avg}. We set the broadening to $5\delta_{\mathrm{avg}}$ to satisfy this criterion but we note that perturbing the Lorentzian broadening has significant influence on the AF-predicted thermal conductivities. For example, changing the broadening by 20 % changes the AF-predicted thermal conductivity for a-C by ∼13 %. Therefore, for a more accurate prediction of thermal conductivity for disordered solids, the readers are referred to Refs. 11 and 12 for a more comprehensive and robust model to describe heat conduction in similar structures.

---

[*] ag4ar@virginia.edu

[†] phopkins@virginia.edu

[1] A. Feldman, High Temperatures – High Pressures **31**, 293 (1999).

[2] P. E. Hopkins, J. R. Serrano, L. M. Phinney, S. P. Kearney, T. W. Grasser, and C. T. Harris, J. Heat Transfer **132**, 081302 (2010).

[3] D. G. Cahill, Rev. Sci. Instrum. **75**, 5119 (2004).

[4] J. L. Braun, D. H. Olson, J. T. Gaskins, and P. E. Hopkins, Rev. Sci. Instrum. **90**, 024905 (2019).

[5] J. R. Maple, U. Dinur, and A. T. Hagler, Proc. Natl. Acad. Sci. **85**, 5350 (1988).

[6] H. Sun, Macromolecules **28**, 701 (1995).

[7] J. R. Olson, K. A. Topp, and R. O. Pohl, Science **259**, 1145 (1993).

[8] L. Chen, X. Wang, and S. Kumar, Sci. Rep. **5**, 12763 (2015).

[9] S. Kumar, C. Shao, S. Lu, and A. J. H. McGaughey, Phys. Rev. B **97**, 104303 (2018).

[10] M. P. Allen and D. J. Tildesley, *Computer simulation of liquids (Oxford Science Publications)*, reprint ed., Oxford science publications (Oxford University Press, 1989).

[11] L. Isaeva, G. Barbalinardo, D. Donadio, and S. Baroni, Nat. Commun. **10**, 3853 (2019).

[12] M. Simoncelli, N. Marzari, and F. Mauri, Nature Physics **15**, 809 (2019).